Physics Letters B 838 (2023) 137684

Contents lists available at ScienceDirect

Physics Letters B

journal homepage: www.elsevier.com/locate/physletb

Electron screening in palladium

A. Cvetinović [a,*], D. Đeorđić [b,c], G.L. Guardo [d,e], M. Kelemen [a,c], M. La Cognata [d], L. Lamia [d,e,f], S. Markelj [a], U. Mikac [a], R.G. Pizzone [d], T. Schwarz-Selinger [g], I. Tišma [a,h], M. Vencelj [a], J. Vesić [a], M. Lipoglavšek [a]

[a] Jožef Stefan Institute, Ljubljana, Slovenia
[b] University of Banja Luka, Faculty of Mechanical Engineering, Banja Luka, Bosnia and Herzegovina
[c] Jožef Stefan International Postgraduate School, Ljubljana, Slovenia
[d] INFN-Laboratori Nazionali del Sud, Catania, Italy
[e] Dipartimento di Fisica e Astronomia "E. Majorana", University of Catania, Catania, Italy
[f] Centro di Fisica Nucleare e Struttura della Materia, University of Catania, Catania, Italy
[g] Max Planck Institute for Plasma Physics, Garching, Germany
[h] Ruđer Bošković Institute, Zagreb, Croatia

ARTICLE INFO

Article history:
Received 31 May 2022
Received in revised form 22 December 2022
Accepted 9 January 2023
Available online 12 January 2023
Editor: D.F. Geesaman

ABSTRACT

The electron screening effect was studied in the $^{1}H(^{7}Li,\alpha)^{4}He$, $^{1}H(^{19}F,\alpha\gamma)^{16}O$ and $^{2}H(^{19}F,p)^{20}F$ nuclear reactions on two different hydrogen-containing palladium foils. In one of the targets we did not detect a large enhancement of the cross section due to electron screening, and in the second one we measured a high electron screening potential for all three reactions, up to an order of magnitude above the theoretical models. Contrary to the predictions given by the available theories, the data suggest that the reason behind this difference is linked to a dependence of the electron screening potential on the host's crystal lattice structure and the location of the target nuclei in the metallic lattice.

© 2023 The Authors. Published by Elsevier B.V. This is an open access article under the CC BY license (http://creativecommons.org/licenses/by/4.0/). Funded by SCOAP[3].

1. Astrophysical motivation

In nuclear reactions that are induced by charged, low-energy particles, atomic electrons can participate in the process by screening the nuclear charge, effectively reducing the repulsive Coulomb barrier and leading to an increase in the measured cross section at Gamow energies. Several theoretical models describing this effect are available (see [1–6] and references therein). The simplest model describing the electron screening effect [1,2] is a rather simple approach, employing a static approximation that assumes unchanged electron densities between the interacting nuclei. Only free atoms are considered and all the effects of lattice periodicity in the ion distributions and binding of the atoms are ignored in these references. This model gives the theoretical upper limit [7] for the electron screening potential (U_e) called the adiabatic limit [2]. However, over the period of past 20 years, many research groups (see Refs. [6,8–14] and references therein) have reported extremely high values for the electron screening potential, much higher than the adiabatic limit. Experimental results show that the cross section is especially enhanced in cases when the target nuclei are implanted into a solid lattice, often more than an order of magnitude above predictions. However, when gaseous targets are used, the electron screening potential remains within the adiabatic limit [9]. Moreover, the inclusion of additional effects [7] and models including quantum-mechanical correlation functions for strongly coupled astrophysical plasmas [3], the dynamically treated electron wave functions in the time-dependent Hartree-Fock scheme [4] and dielectric-function method which allows to treat the electron screening as a static polarization of the metallic medium induced by the positively charged particle [6], were not able to explain experimental observations. Even in the cases of indirect methods that measure the bare nucleus cross section, e.g. Trojan Horse Method [15], values above the adiabatic limit are often observed (see Ref. [16] and references therein).

Measurements report a strong dependence of the screening potential on the target host material, proton number Z of the projectile [14], the target nuclei concentration [9] crystal lattice defects and presence of impurities [17], indicating that the reaction rate could depend on the host's crystal lattice structure and the position of trapped target nuclei in it. Although the dielectric function theory supports the target material dependence of the screening potential [12,17], the theoretical prediction agrees only with experimental data for virgin metallic samples, where a small screening effect was measured. However, the crystal defects induced by a

* Corresponding author.
E-mail address: aleksandra.cvetinovic@ijs.si (A. Cvetinović).

https://doi.org/10.1016/j.physletb.2023.137684
0370-2693/© 2023 The Authors. Published by Elsevier B.V. This is an open access article under the CC BY license (http://creativecommons.org/licenses/by/4.0/). Funded by SCOAP[3].

long-term irradiation or mechanical stress of the target significantly increase the experimental values of the screening potential. The study of Refs. [18,19] investigating electron screening in deuterium-implanted targets attributed the cross-section enhancement partly to a channelling effect. However, this could be the case if monocrystalline targets were used, but most experiments measuring high electron screening (including ours) were conducted on polycrystalline targets.

Understanding electron screening is very important in nucleosynthesis calculations. Precise reaction rates should be known at very low energies where screening effects cannot be neglected and for a proper application, electron screening must be included in most calculations related to the nucleosynthesis of elements. However, this is currently impossible because we simply do not know enough about this effect. Furthermore, it is believed that electron screening in stellar plasmas differs from the laboratory screening because the atoms in the stellar interiors are in most cases in highly stripped states and the nuclei are immersed in a sea of almost free electrons, which tend to cluster closer to the nucleus than in atoms. A classical theory [5] on electron dynamics, together with the simple view of Ref. [2], as well as different approaches describing weakly and strongly coupled plasmas, taking into account classical and quantum mechanical effects [20] were employed to describe electron screening in plasma. Unfortunately, there is no way to check whether such extremely simplified assumptions are actually valid. At present, stellar conditions cannot be simulated in the laboratory (this could be achievable in some future facilities) and at the moment, there is no existing possibility to study the screening effect in stellar plasmas. Bearing in mind that the theory behind electron screening is unknown, the natural course of things is to perform experiments that will increase the knowledge to a sufficiently high level to understand the effect, and at present, the only available strategy is to study electron screening in materials already available in the laboratory.

To simplify the analysis, when nuclear reactions are studied at low energies, the cross section σ is usually defined using the astrophysical $S(E)$-factor, which in the case of non-resonant reactions varies smoothly with energy [21]:

$$\sigma(E) = \frac{S(E)}{E} e^{-2\pi\eta}. \tag{1}$$

Here η is the Sommerfeld parameter and E denotes the centre-of-mass energy. Taking into account electron screening and according to the suggestions given by Huke et al. [12], the enhancement factor f of the nuclear reaction cross section can be defined as the ratio of the screened (σ_s) and bare-nucleus (σ_b) cross sections:

$$f(U_e) = \frac{\sigma_s}{\sigma_b} = exp\left[Z_1 Z_2 e^2 / 2\epsilon_0 \hbar \left(\sqrt{\frac{\mu}{2E}} - \sqrt{\frac{\mu}{2(E+U_e)}} \right) \right], \tag{2}$$

where Z_1 and Z_2 are the charge numbers of interacting nuclei and μ is the reduced mass.

Our group has been investigating electron screening for several years already [13,14,22,23]. We measured the largest electron screening effect in inverse kinematics (up to a factor of 50 above the adiabatic limit, as measured in a graphite target [14]), while in normal kinematics there was no indication of large electron screening, except for the p+d reaction [23]. The results that are published in another paper [24] describing high screening potentials measured in metallic compared to insulating targets in normal kinematics with a proton beam on ^{50}V and ^{176}Lu targets, could not be confirmed by our group [22]. Our findings suggested that the preparation of the target can influence electron screening, pointing to a dependence of electron screening potential on the location of the target nuclei in a metallic lattice. Since these findings cannot be explained by the theory based on static electron densities, we proposed an idea which assumes that an electron is caught in the attractive potential of two approaching nuclei, similar to the potential of a hydrogen molecular ion (for more details see [14]). Moreover, we recently observed a new type of nuclear reaction [23] supporting our approach to electron screening effect when we looked at the proton-induced nuclear-fusion reaction on deuterium implanted in a graphite target, which normally produces a ^{3}He nucleus and a γ-ray. However, based on our approach, due to the electron screening in graphite, sometimes an electron with discrete energy can be emitted instead of a γ-ray. The paper by M. Lipoglavšek et al. [23] confirms that such electrons are emitted, showing that orbital electrons do not just lower the Coulomb barrier from an atomic shell, but actively participate in the reaction at a much closer distance than the atomic radius. However, this new nuclear reaction was only observed for a single beam energy and in a single target. Therefore, to confirm that our approach to electron screening is correct, new studies are required.

Lately, our group was focusing on studying the electron screening effect in palladium targets. Pd has the ability to absorb large volumetric quantities of hydrogen at room temperature and atmospheric pressure. Due to this, Pd is considered as a very attractive material for hydrogen storage and transportation. It is also well known that PdH_x system does not behave like a stoichiometric compound but like a homogeneous alloy in which the dissolved H plays the role of an alloy partner. Based on our previous findings suggesting that the preparation of the host material and location of the target nuclei in the metallic lattice can influence the electron screening, our goal was to find different values of U_e in two palladium targets and then to understand which parameters of those targets differ and cause high electron screening. We also investigated the dependence of the electron screening potential on the atomic number Z of the projectile. In order to get a better insight into the condition of the palladium lattice itself, targets were analysed by Nuclear Reaction Analysis (NRA) technique, X-ray diffraction and a Nuclear Magnetic Resonance (NMR) analysis. The latest results from our research and the applied methodology are presented below.

2. Experimental setup and target preparation

The experimental study of the electron screening effect was performed using the 2 MV Tandetron accelerator at the Microanalytical Center of Jožef Stefan Institute (JSI). We investigated the dependence of the electron screening potential on the atomic number Z of the projectile by measuring the rates of the ^{1}H(^{7}Li,α)^{4}He, ^{1}H(^{19}F,$\alpha\gamma$)^{16}O and ^{2}H(^{19}F,p)^{20}F reactions on two different hydrogen-containing palladium targets.

Alpha particles emitted from the ^{7}Li(p,α)^{4}He reaction were detected by a 500 µm thick passivated implanted planar Si (PIPS) detector with an active area of 300 mm^2, placed 52 mm from the target at an angle of 135° compared to the direction of the ^{7}Li ion beam (see the scheme of the experimental setup in Fig. 1). The detector was calibrated using an ^{241}Am α-particle source, and we obtained a geometric efficiency of 0.0876%. In order to prevent scattered beam particles from hitting the detector, a 3 µm thick Al absorber was placed in front of the PIPS detector. The electronic threshold was set at 50 keV.

The γ-rays with energies of 6129 keV (produced from ^{16}O decay to the ground state in the ^{19}F+p reaction) [25] and 1634 keV (emitted in the ^{20}Ne de-excitation to the ground state from ^{20}F β^- decay) [26] were detected using a High-Purity Germanium (HPGe) detector positioned 57 mm from the target at an angle of 135° with respect to the ^{19}F ion beam direction (see Fig. 1). The intrin-

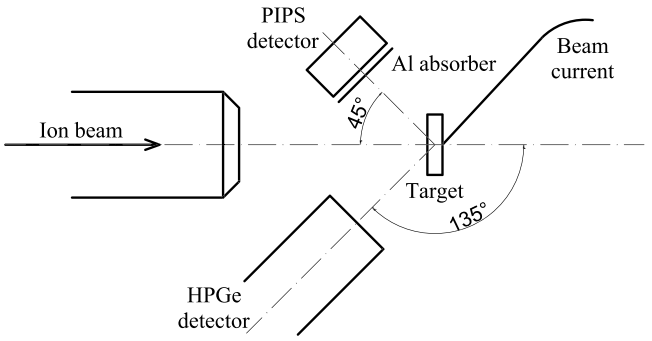

Fig. 1. The scheme of the experimental setup used for the experiments performed in inverse kinematics.

sic detector efficiency was 53% relative to a 3″ by 3″ NaI detector and it had an efficiency of 0.6% and a resolution of 2.2 keV at the 1.3 MeV ^{60}Co peak. The HPGe detector efficiency at higher energies was evaluated using a Monte Carlo simulation provided by the detector manufacturer (Canberra).

The ^{7}Li+p reaction was measured in an energy region between 0.437 and 2.071 MeV of the ^{7}Li ion beam with a beam current of about 0.3 μA. The ^{19}F ion beam with currents of about 0.5 μA was used to study the ^{19}F+p reaction in an energy region between 6.410 and 6.819 MeV and the ^{19}F+d reaction in an energy region between 3.089 and 9.200 MeV. The numbers of incident ions were deduced by measuring the charge collected on the electrically isolated target chamber. In order to correct the detected yields for the background α-particle and γ-ray activity present in the laboratory, the background spectra were observed in both detectors for several days without beam.

Two 2×2 cm palladium targets were used. The first target was Chempur's 100 μm thick soft Pd foil and the second one was a 100 μm thick cold rolled Pd foil produced according to our specifications at Zlatarna Celje. It was cold rolled from a thickness of about 2.5 mm to 0.1 mm. This foil was much less flexible than Chempur's one. The purities of both foils were above 99.9%. In order to prepare the targets for electron screening studies, both foils were first loaded and unloaded with hydrogen several times. The cycling was performed by leaving the palladium in hydrogen gas at the pressure of 1 bar and temperature of 24 °C for 24 hours and then heating it to 300 °C. After that, the Pd foils were once again loaded, but this time the foils were left in a gas mixture containing 85% deuterium and 15% hydrogen, again at the pressure of 1 bar and a temperature of 24 °C for 24 hours.

In order to effectively prevent substantial heating of the targets during the experiment, prepared palladium foils were mounted on a massive copper holder. Targets were positioned in a high vacuum chamber perpendicularly to the beam direction. During the experiment, we monitored hydrogen and deuterium loss in both targets by repeatedly measuring yields at the beam energies of 2.071, 6.665 and 7.671 MeV for the ^{7}Li+p, ^{19}F+p and ^{19}F+d reactions, respectively, before and after each measurement at other energies. Almost negligible changes in hydrogen concentration were detected in both palladium targets in experiments with the ^{7}Li+p and ^{19}F+p reactions. However, our targets showed loss of deuterium (and hydrogen, consequentially) during all measurements in the experiment with the ^{19}F+d reaction due to higher beam intensities and longer measurements. In order to correct for the deuterium loss, we normalized the detected yields for a given beam energy to the average of the two control measurements at the energy of 7.671 MeV.

To determine the deuterium depth distribution, we performed quantitative deuterium depth profiling with the Nuclear Reaction Analysis (NRA) technique for each target. For this purpose, high energy protons emitted in the ^{2}H(^{3}He,p)^{4}He reaction were measured at six ^{3}He energies, in an energy region from 0.629 to 4.297 MeV. A uniform deuterium depth distribution was found in both targets even after targets were bombarded with energetic ^{19}F ion beam causing D(H) evaporation. The deuterium depth profiles were obtained by fitting the NRA spectra using the SIMNRA code [27]. Fig. 2 shows deuterium depth distributions measured in our hard and soft Pd foils after the ^{19}F+d experiment. The depth profile shows uniform deuterium concentrations within error bars, down to a depth of 7 μm. Note that the 2.071 MeV ^{7}Li ion beam is fully stopped in palladium at the depth of 1.92 μm and the 9.200 MeV ^{19}F ion beam is fully stopped at the depth of 2.06 μm [28]. Since we do not expect the two hydrogen isotopes to behave differently when loaded simultaneously in palladium foils, we assumed a uniform depth distribution for protons, too.

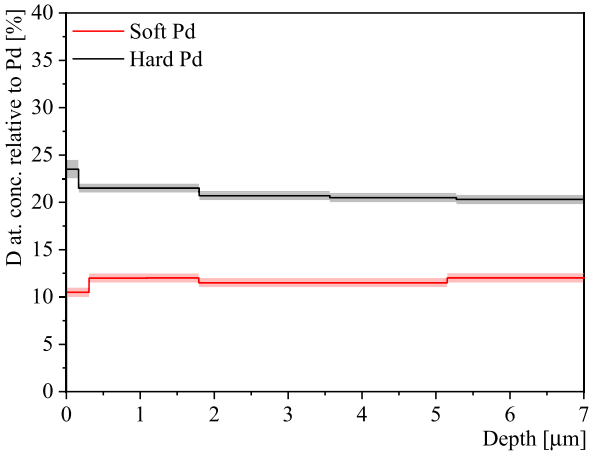

Fig. 2. Deuterium concentration relative to Palladium as a function of depth in the target, measured in soft Pd (red line) and hard Pd (black line) foils using the Nuclear Reaction Analysis technique. Shaded areas represent errors to the fitted deuterium concentrations obtained using SIMNRA code [27].

Total hydrogen/deuterium concentration in the targets could be precisely determined gravimetrically by subtracting the weight of the empty foil from the weight of the filled one. Stoichiometries deduced in this way agreed very well with the NRA measurements. Although, both of our targets had uniform H(D) distribution and were loaded with H(D) at the same time in the same gas chamber, in the soft palladium foil, maximum concentrations of 70% of H(D) per metallic atom were achieved. This is consistent with the limit of hydrogen absorption at normal pressures [29] when approximately 70% of the octahedral holes are occupied. However, the cold rolled (hard) foil could be loaded only up to 47% of H(D) per metallic atom, showing already a different behaviour of this target.

3. Data analysis

The two palladium targets, prepared in the way presented above, were used to study the electron screening effect by measuring the ^{1}H(^{7}Li,α)^{4}He, ^{1}H(^{19}F,$\alpha\gamma$)^{16}O and ^{2}H(^{19}F,p)^{20}F reaction rates. The description of the applied procedure follows.

3.1. Electron screening in the ^{19}F+d reaction

First, we investigated electron screening in Pd targets by studying the ^{2}H(^{19}F,p)^{20}F reaction, where the produced radioactive isotope ^{20}F decays with a half-life of 11 s [26]. After the β-decay, a γ-ray with an energy of 1634 keV is emitted with a branching ratio of 99.1% [26]. A part of a typical spectrum in the energy window of interest is shown in Fig. 3. According to the definition of

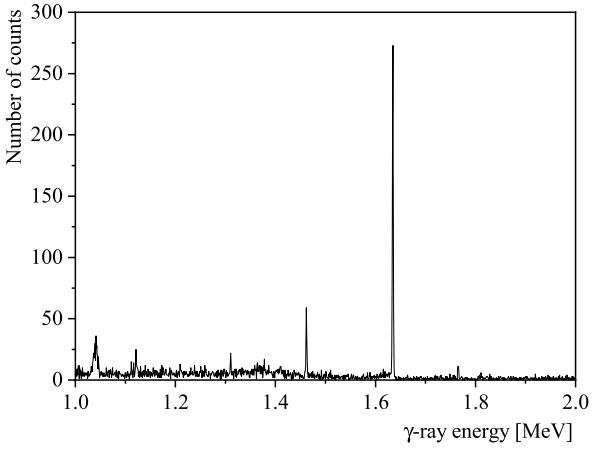

Fig. 3. Part of a γ-ray spectrum with the peak at the energy of 1.634 MeV emitted in the ^{2}H(^{19}F,p)^{20}F reaction at fluorine beam energy E_F=7.671 MeV observed on the hard Pd target.

the cross section σ in the case of a thin target [30], the experimentally measured γ-ray yield N_γ is defined by the equation:

$$N_\gamma = \sigma \epsilon W_\gamma N_F n_D \frac{\rho N_A x}{M}, \tag{3}$$

where ϵ is the efficiency of the detector, W_γ is the angular distribution factor for emitted γ-rays, N_F is the number of incident ^{19}F ions and the value $n_D \frac{\rho N_A d}{M}$ represents the surface density of deuterium atoms in the target (here n_D is the number of deuterium atoms per crystal lattice atom, x is the target thickness, N_A, ρ and M are the Avogadro's number, target density and molar mass).

Since the ^{2}H(^{19}F,p)^{20}F reaction does not have any known resonances in the fluorine energy range between 3 and 9 MeV, the γ-ray yield for the thick-target had to be calculated by transforming Eq. (3) into a differential form and integrating over energies from the beam energy E_0 to 0:

$$N_\gamma = N_F n_D \frac{\rho N_A}{M} \int_{E_0}^{0} \epsilon W_\gamma \frac{\sigma_E}{dE_F/dx} dE_F. \tag{4}$$

The stopping power dE_F/dx was calculated using SRIM code [28] and the γ-ray angular distribution is isotropic after β decay [26].

3.1.1. The bare ^{19}F+d reaction cross section

To calculate the electron screening potential from our experimental data, we need to take into account the bare-nucleus cross section. However, there is no available cross section for the ^{19}F+d reaction in the studied energy region. To determine the bare-nucleus cross section, we measured the same reaction, but this time in normal kinematics, in which we never observed a large electron screening effect, except for the p+d reaction [22,23]. The measurement was performed at Max Planck Institute for Plasma Physics in Garching. We used the deuterium ion beam accelerated with the 3 MV accelerator in an energy region from 303 to 998 keV incident on an 8 and an 85 nm thick CaF_2 targets positioned perpendicularly to the beam. The 1634 keV γ-ray yield was measured using the same HPGe detector as was used for the experiments in inverse kinematics.

To increase the detection efficiency, we increased the solid angle by positioning the detector as close to the target as possible. To accomplish this, we mounted the detector on the outer side of the vacuum chamber wall while the target was mounted on the opposite (inner) side of the wall, so between the target and the detector was only 4.82 mm thick stainless steel. The detector was positioned at an angle of 0° with respect to the ion beam direction. The number of incident ions were deduced from the Rutherford backscattering (RBS) spectra recorded in an RBS detector, positioned 42.3 cm from the target at an angle of 177° with respect to the beam direction, and cross-checked with the mesh current integrator positioned behind it. The RBS detector was a 50 μm thick PIPS detector with a diameter of the aperture of 5 mm. The energy resolution of the detector was 20 keV. A scheme of the experimental setup is given in Fig. 4. The RBS spectra were analysed using SIMNRA code [27].

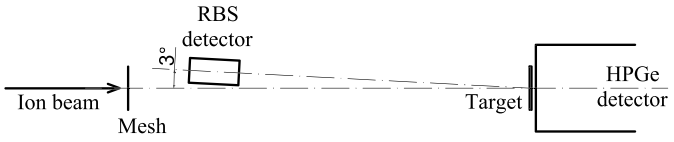

Fig. 4. The scheme of the experimental setup used for the experiment performed in normal kinematics.

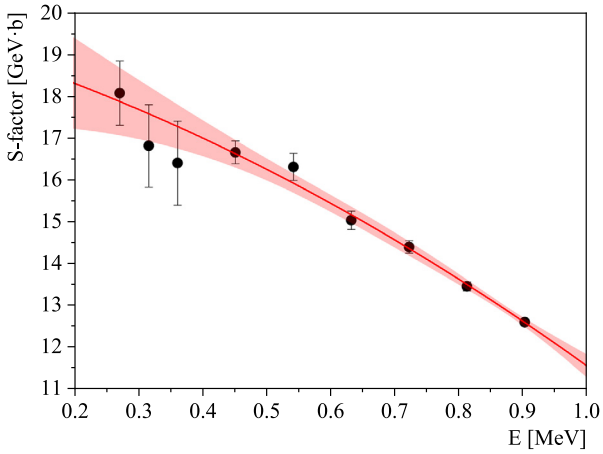

Fig. 5. The astrophysical S-factor for the ^{19}F(d,p)^{20}F reaction as a function of the centre-of-mass energy E. Black points represent the experimental data and the red solid line represents a least-squares fit to the data using a parabola. Red shaded area is the 95% confidence band to the fit.

The resulting astrophysical S-factor as a function of the centre-of-mass energy is given in Fig. 5. Error bars include only statistical errors. An estimated systematic error includes the uncertainty on stopping power (10%), hydrogen concentration in the target (4%) and the detector efficiency (4%). However, this will not impact screening potential values since all points would be shifted in the same direction. The experimental points were fitted with a parabola and from the least-squares fit to the data we obtained:

$$S(E)_{^{19}F+d} = 19380 - 4596E - 3218E^2\,[MeVb], \tag{5}$$

when the centre-of-mass energy E is given in MeV.

In the next step, by combining Eq. (1) and Eq. (4) and taking Eq. (5) for the astrophysical S-factor, we got a new function that we used to fit γ-ray yields measured in palladium targets in inverse kinematics. The electron screening potential U_e was left as the only free parameter in the fitting procedure. Resulting from the one-parameter least-squares fit to the data, we obtained a large electron screening potential, U_e=18.2±3.3 keV (see Table 1), in our hard Pd target. However, the screening potential in our soft Pd foil was comparable with adiabatic limit, within error bars, U_e=3.2±1.9 keV. In the upper panel of Fig. 6 we show the integrated enhancement factor as a function of fluorine beam energy in the centre-of-mass system that we obtained in the hard pal-

Table 1
The electron screening potentials U_e measured in the ^{1}H(^{7}Li,α)^{4}He, ^{1}H(^{19}F,$\alpha\gamma$)^{16}O and ^{2}H(^{19}F,p)^{20}F reactions in the hard Pd target in comparison with predicted screening potentials given by the adiabatic model.

Reaction	U_{ad} [keV]	U_e [keV]	$\frac{U_e}{U_{ad}}$
^{7}Li+p	0.24	2.86±0.19	12
^{19}F+p	2.19	18.7±1.5	8.5
^{19}F+d	2.19	18.2±3.3	8.2

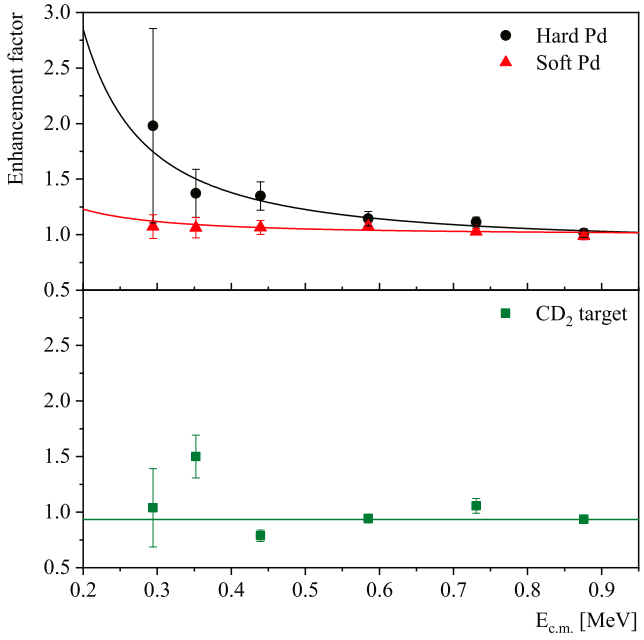

Fig. 6. Integrated enhancement factors as a function of fluorine beam energy in the centre-of-mass system for the ^{2}H(^{19}F,p)^{20}F reaction obtained in the hard Pd foil (black points), where the screening potential of U_e=18.2±3.3 keV was obtained, in the soft Pd foil (red triangles) with U_e=3.2±1.9 keV and in the CD_2 target (green squares) where no screening was found. Points represent experimental data and the solid lines represent least-squares fits to the data combining Eq. (1), Eq. (4) and Eq. (5).

ladium target, in comparison to the one measured in the soft Pd target.

Since we do not expect high screening potential to be deduced in insulator targets, we measured the ^{19}F+d reaction in two thin CD_2 foils prepared at the Istituto Nazionale di Fisica Nucleare - Laboratori Nazionali del Sud (INFN-LNS). One of the targets was 94 nm thick and the other one was 138 nm thick target coated with 24 nm of gold. Our original idea was to use these two targets for the bare-nucleus cross section determination. However, the foils were very unstable and blackened very fast due to high beam intensities and high-Z beam, so in the end we opted out for already described experiment to determine the bare-nucleus cross section. Nonetheless, we report here the averaged enhancement factor obtained in two CD_2 targets in the lower panel of Fig. 6. As it can be seen the deduced screening potential was too small to be stated statistically different from zero.

We compared our result with the data available in the literature [31]. This cross section measured in 1950 covers an energy region from 0.7 MeV to 1.796 MeV slightly overlapping with the energy region of our measurements. However, we found out that this cross section is lower than ours by a factor of about 4 in the region where the two measurements overlap, although it has a similar energy dependence.

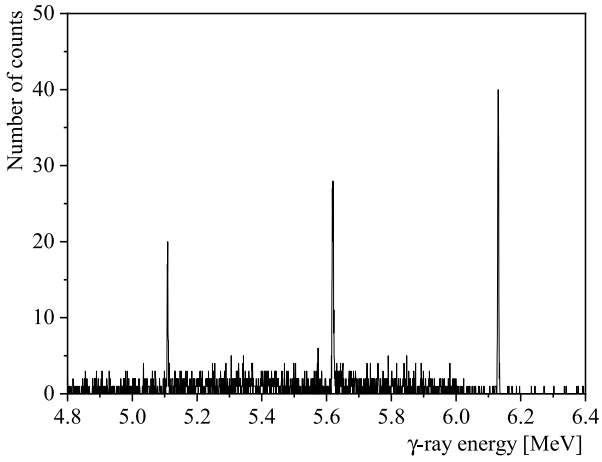

Fig. 7. Part of a γ-ray spectrum with the peak at the energy of 6.129 MeV and its single and double escape peaks emitted in the ^{1}H(^{19}F,$\alpha\gamma$)^{16}O reaction at fluorine beam energy E_F=6.665 MeV observed in the soft Pd target.

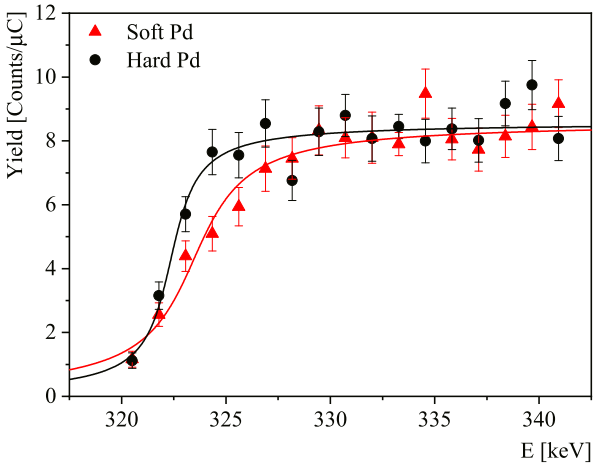

Fig. 8. γ-ray yields for the ^{1}H(^{19}F,$\alpha\gamma$)^{16}O reaction as a function of the centre-of-mass energy, in the soft Pd (red triangles) and the hard Pd (black circles) foils near the resonance energy of 323.31 keV in the centre-of-mass system. The solid lines represent fits with Eq. (6). One can observe that above the resonance energy the measured yields are constant, confirming a uniform hydrogen distribution throughout the analysed target depth of about 70 nm.

3.2. Electron screening in the ^{19}F+p reaction

The ^{1}H(^{19}F,$\alpha\gamma$)^{16}O reaction was studied by measuring the narrow resonance (Γ= 2.34(4) keV) at E_r=323.31 keV [32] in the centre-of-mass system by detecting γ rays at the energy of 6128.6 keV (see Fig. 7) produced from ^{16}O decay to the ground state [25]. This low energy resonance is very well isolated and relatively strong, making it suitable for electron screening studies. Since the range of ^{19}F ions was smaller than the target thickness, we observed step-like shaped resonances that are described by the infinitely tick target yield Y given by [21]:

$$Y = \frac{\lambda^2 \omega\gamma}{2\pi\epsilon_r}\left[arctan\left(\frac{E-E_r}{\Gamma/2}\right)+\frac{\pi}{2}\right]. \quad (6)$$

Here λ is the de Broglie wavelength of the beam and ϵ_r is its effective stopping power in the target, calculated with the SRIM code [28], $\omega\gamma$ is the resonance strength and Γ is the resonance width.

The experimentally measured and fitted yields for the ^{1}H(^{19}F,$\alpha\gamma$)^{16}O reaction in both palladium targets are shown in Fig. 8 as a function of beam energy around the resonance energy of 323.31 keV in the centre-of-mass (or 6417.9 MeV in the labo-

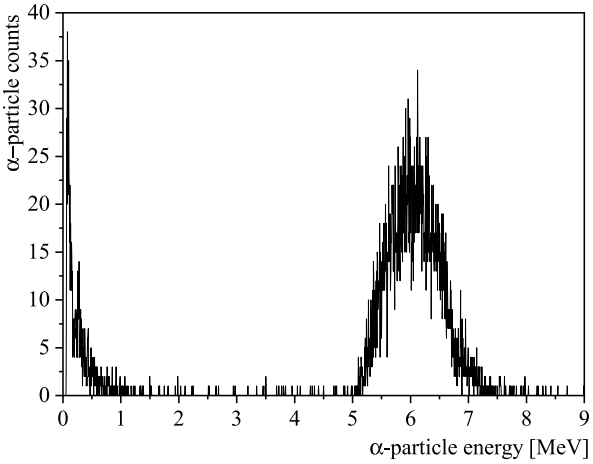

Fig. 9. The α-particle spectrum obtained for the hard Pd target at ^{7}Li beam energy of 1.05 MeV. The counts in the energy window from about 5 to 7 MeV correspond to α particles from the ^{7}Li+p reaction.

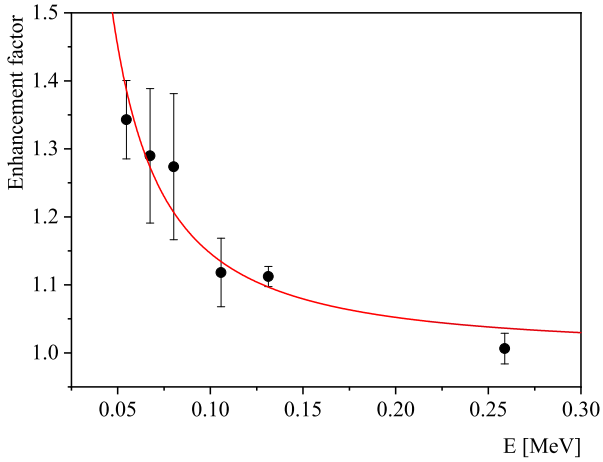

Fig. 10. The integrated enhancement factor as a function of centre-of-mass energy for the ^{1}H(^{7}Li,α)^{4}He reaction in the hard Pd target. Black points represent the experimental data and the red solid line represents a least-squares fit using Eq. (2) returning U_e=2.86±0.19 keV.

ratory) system. Due to the presence of a thin oxide layer on the surface of our soft Pd foil, the obtained resonance thickness in this target was larger than the one reported in the literature.

Since $\omega\gamma$ is proportional to σ [21]:

$$\sigma(E) = \frac{\lambda^2 \omega\gamma}{2\pi\Gamma}, \tag{7}$$

the enhancement factor was calculated, according to Eq. (2), as:

$$f(U_e) = \frac{\omega\gamma_s}{\omega\gamma_b}. \tag{8}$$

The $\omega\gamma$ for the soft Pd target was taken as the bare resonance strength, in accordance with results obtained from the ^{19}F+d reaction, where no large electron screening was found in this target. Therefore, for the enhancement factor we calculated a value of f=1.53±0.05 which corresponds to the electron screening potential of U_e=18.7±1.5 keV (see Table 1). This result is in agreement with the one obtained for the ^{19}F+d reaction, confirming the isotopic invariance of electron screening expected from the adiabatic model [2].

Since the measured yields depend on the resonance energy, the surface hydrogen concentration is probed at the resonance energy, whereas at higher energies the concentration below the surface is determined due to the ion stopping in the target. One can observe that above the resonance energy the measured yields are constant, confirming a uniform hydrogen distribution throughout the analysed target depth of about 70 nm. This is in agreement with results for deuterium depth distribution obtained from NRA.

3.3. Electron screening in the ^{7}Li+p reaction

The detected number of α particles N_α from the ^{7}Li(p,α)^{4}He reaction was deduced by subtracting the background from the recorded spectra and counting the number of α-particles in the correct energy window for each beam energy. This was possible due to the simplicity of the spectra which is reflected in the fact that background radiation and noise were low in a wide energy window around the energies corresponding to α particles from the studied reaction. An example of the α-particle spectrum is shown in Fig. 9.

By modifying Eq. (3) in an appropriate form:

$$N_\alpha = 2\sigma W_\alpha N_{Li} n_H \frac{\rho N_A x}{M}, \tag{9}$$

where W_α is the angular distribution factor for emitted α particles, N_{Li} is the number of incident ^{7}Li ions and the value $n_H \frac{\rho N_A d}{M}$ represents the surface density of the hydrogen atoms in the target. The factor of 2 in this equation takes into account two identical α-particles emitted in the observed reaction.

The ^{7}Li(p,α)^{4}He reaction does not have any known resonances in the lithium energy range between 0.4 and 2 MeV. Therefore, the α-particle yields for the thick-target with homogeneous distribution of hydrogen, similar to the ^{19}F+d case, had to be calculated by transforming Eq. (9) into a differential form and integrating over energies from the beam energy E_0 to 0:

$$N_\alpha = 2N_{Li} n_H \frac{\rho N_A}{M} \int_{E_0}^{0} \epsilon\omega_\alpha \frac{\sigma_E}{dE_{Li}/dx} dE_{Li} \tag{10}$$

and combining it with Eq. (1). The stopping power dE_{Li}/dx was calculated using SRIM code [28] and the α-particle angular distribution was taken from Ref. [33].

Assuming that there is no high screening potential in our soft Pd target, we calculated an enhancement factor in hard Pd by dividing the reaction yields of the two targets. Our data were then fitted by Eq. (2) with the electron screening potential U_e left as the only free parameter. Resulting from the one-parameter least-squares fit to the data we obtained the screening potential U_e=2.86±0.19 keV (see Table 1). Fig. 10 shows the integrated enhancement factor as a function of centre-of-mass energy in our hard Pd target.

4. Discussion

The first goal of this study was to fabricate at least two palladium targets with different electron screening and then to understand which parameters of those targets differ. Thus, one of our targets was a soft Pd foil in which we measured low screening, and the second one was a cold rolled (hard) foil where we measured a high screening potential that is an order of magnitude above the adiabatic model calculation. In normal Pd, the absorbed H(D) atoms occupy octahedral interstitial sites of the face-centred cubic (fcc) lattice [34]. H(D) in palladium lattice can also get trapped at grain boundaries, dislocations and voids [35]. It is well known that the cold rolling process increases the number of grain boundary defects, but when the foil is annealed the number of these defects is reduced. As it was discussed already in Ref. [14], a pos-

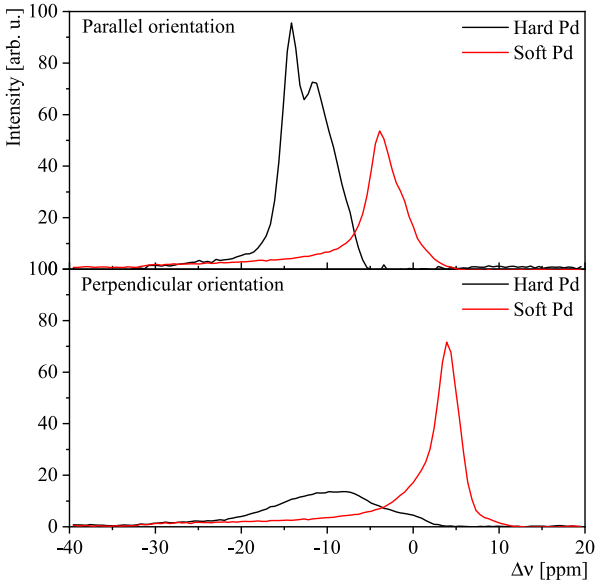

Fig. 11. ^{1}H NMR lineshapes measured by Hahn echo at ν_0=100 MHz of our soft and hard Pd foils oriented parallel (upper panel) and perpendicular (lower panel) to applied static magnetic field. A broad line at ≈-28 ppm is the background signal from the NMR probe.

sible explanation for this different behaviour of the two foils could be that the screening potential is increased by increasing the number of grain boundary defects into which hydrogen and deuterium atoms could be trapped. As we have shown in Ref. [13], hydrogen on regular interstitial sites in the fcc lattice did not produce a large electron screening effect. Only when the H(D) atoms are pulled away from their fcc equilibrium positions a large screening effect occurred. At octahedral interstitial sites the electron density is the lowest in the fcc lattice, while when hydrogen nuclei are pulled away from these sites, they are placed on the path of valence electrons. These then determine the screening potential. To substantiate this claim and to elucidate positions of hydrogen isotopes in palladium lattice and local electronic structure around H(D), we measured the Knight shift by employing the nuclear magnetic resonance (NMR) technique [36].

The Knight shift originates from the interaction of conducting electrons in metals with nuclear spins. It includes three main contributions [36,37]:

$$K = K_{Pauli} + K_{dia} + K_{orb}. \tag{11}$$

The first term includes isotropic and anisotropic effects, directly by contact and spin dipolar interactions, and indirectly via core polarization and polarization of conduction band electrons below the Fermi level and is proportional to the average probability density at the nucleus site for all electronic states at the Fermi level $N(E_F)$. The K_{dia} and K_{orb} are the orbital paramagnetic and diamagnetic terms.

The ^{1}H NMR lineshapes were measured at 2.35 T (equivalent to ν_0=100 MHz proton frequency). Our two Pd foils with initial H/Pd concentration of 0.70 and 0.47, respectively were inserted in the rf coil and two sides were fixed to a Teflon holder. The Hahn echo [36] pulse sequence ($\pi/2$-τ-π-τ-echo) was used with the $\pi/2$ rf pulse length of 8 μs and the inter-echo time τ of 60 μs. To be able to obtain the real proton Knight shift K_H without the contribution of the demagnetizing field, which is due to the overall macroscopic sample shape, the experiments were performed with foils parallel and perpendicular to the applied static magnetic field. Obtained results are given in Fig. 11 showing an obvious difference

Table 2
Knight shifts in ppm for soft and hard Pd foils relative to water standard in comparison with the theoretical shift K_{H_t} [40].

Foil	n_D	K_{H_1} [ppm]	K_{H_2} [ppm]	K_{H_t} [ppm]
Soft Pd	0.70	26.7	/	≈18
Hard Pd	0.47	20.2	15.6	≈-14

in the frequency shift between the two foils clearly indicating different electron densities at hydrogen nuclei. While in the soft Pd foil most protons are at the same position in the crystal lattice, in the hard Pd foil they are placed at least at two different positions. Assuming that our foils can be approximated by infinite sheets and that the symmetry of the electron environment of the ^{1}H spins is cubic, the true Knight shift is given by [38,39]:

$$K_H = S(0°) - \frac{4\pi}{3}\chi_\nu - \sigma, \tag{12}$$

where S(0°) is the shift at a parallel position with respect to the static magnetic field B_0, χ_ν is the bulk susceptibility of the sample that can be expressed as χ_ν=[S(0°)-S(90°)]/4π and σ is the frequency of the non-metallic reference material, i.e. the water protons in our case. Measured Knight shifts for the two Pd foils are given in Table 2. The obtained K_H for hydrogen in the soft Pd foil is in good agreement with the theoretical Knight shift value for $PdH_{0.7}$ [40]. The K_H values for the hard Pd foil, however, differ from the theoretical value, that is approximately -14 ppm for $PdH_{0.47}$. This discrepancy shows that the majority of hydrogen atoms are not located at regular octahedral interstitial sites in the hard Pd foil, but mainly at crystal lattice defects. It is well known that the cold rolling process creates a large number of grain boundary defects into which hydrogen and deuterium atoms could be trapped, but when the foil is annealed the number of these defects is reduced. The fact that our hard Pd foil was cold rolled, indicates that an increased number of defects can play an important role in the screening mechanism. Namely, the difference of about 30 ppm points to a substantially higher density of electronic states at the position of the protons in the hard Pd foil.

One of the main goals of the present study was also to investigate the dependence of electron screening on the atomic number Z of the projectile. So, the reactions with ^{7}Li and ^{19}F ion beams (Z=3 and 9) were studied. From Table 1 one can find that this dependence seems to be closer to quadratic than linear one expected from Ref. [24]. The quadratic dependence coincides with the Z-dependence of the ionization energy of single electron ions [41].

Additionally, to check the isotope effect of electron screening, we studied two reactions induced with the ^{19}F ion beam - ^{19}F+p and ^{19}F+d. As can be seen from Table 1 no such dependence was found. This is in agreement with the theory [2].

Since the results critically depend on the stopping powers, we checked whether SRIM [28] used experimental data or calculated stopping powers and differences between the two. For the Li beam, measurements exist in Pd and cover a range of energies from about 5 MeV down to 1 MeV [42]. The agreement with calculations is good and the differences between the measured and the calculated stopping powers are less than 2.5%. For the F beam in Pd measurements exist in a narrow energy region from 80 keV to 400 keV [43], but the neighbouring carbon and oxygen cover the energies from 1 MeV to 5 MeV [44] and from 1.5 MeV to 4 MeV [45], respectively. The differences between the measured and calculated stopping powers are never larger than 15%. There are many more measurements of stopping powers in neighbouring Ag metal. Also, in this metal the vast majority of measurements agrees with theory by better than 15% [28]. From this it is clear that the obtained enhancement factors cannot be explained by the potential use of wrong stopping powers. Moreover, the different hydrogen content

in different Pd targets changes the stopping powers by less than 1%. Therefore, the use of wrong stopping powers would not change our electron screening potentials by more than 1%.

5. Conclusions

We studied the electron screening effect in the $^{1}H(^{7}Li,\alpha)^{4}He$, $^{1}H(^{19}F,\alpha\gamma)^{16}O$ and $^{2}H(^{19}F,p)^{20}F$ nuclear reactions on two different hydrogen containing palladium foils. In one of our targets we detected electron screening that is in an agreement with the adiabatic limit, and in the second one we measured a high electron screening potentials for all three reactions, that are an order of magnitude above the theoretical model. In order to understand the reason behind this different behaviour of the two foils, we measured the Knight's shift by employing the nuclear magnetic resonance (NMR) technique. The results showed that the target preparation is only an indirect cause of the high screening potentials obtained experimentally. The target preparation influences the position of the target nucleus in the crystal lattice of the host metal and so the electron densities around the implanted target nucleus. Different electron densities are the direct cause for different screening potentials, which is confirmed by measuring very different Knight shifts in our targets. This indicates that contrary to the predictions given by the available theory, the screening effect is not linked to the static electron densities around interacting nuclei and that a new approach has to be applied. We also found that the dependence of electron screening on the atomic number Z of the projectile seems to be closer to quadratic than linear one expected from the theory [2]. We confirmed that there is no isotope dependence of the screening potential.

In order to better understand how electron screening is linked to the host's crystal lattice structures and the location of the target nuclei in the metallic lattice and how electron densities affect it, further studies are required. Since in the stellar plasma, electron densities around the target nucleus are much higher than the ones existing in materials available in the lab, knowing very well the dependence of electron screening on electron densities is crucial in order to draw the parallel with the stellar plasma. It would be advisable to study screening energies with heavier target nuclei implanted in the crystal lattice, such as He or Li. Besides, the same investigations should be repeated with different host materials and additional quantitative methods, such as neutron and X-ray diffraction, should be applied to investigate the positions of target nuclei in the lattice.

Declaration of competing interest

The authors declare that they have no known competing financial interests or personal relationships that could have appeared to influence the work reported in this paper.

Data availability

No data was used for the research described in the article.

Acknowledgements

This work was partially supported by the Slovenian Research Agency under the grant "Electron Screening in Nuclear Reactions" (N1-0089) and partly by the Horizon 2020 Framework Programme under the grant "Clean Energy from Hydrogen-Metal Systems" (951974).

The authors are grateful for the support from the LNS target laboratory for providing CD_2 targets.

References

[1] E.E. Salpeter, Aust. J. Phys. 7 (1954) 373.
[2] H.J. Assenbaum, et al., Z. Phys. A 327 (1987) 461.
[3] S. Ichimaru, Rev. Mod. Phys. 65 (1993) 255.
[4] T.D. Shoppa, et al., Phys. Rev. C 48 (1993) 837.
[5] C. Rolfs, W.S. Rodney, Cauldrons in the Cosmos, University of Chicago Press, Chicago, 1988.
[6] K. Czerski, et al., Europhys. Lett. 68 (2004) 363.
[7] A.B. Balantekin, et al., Nucl. Phys. A 627 (1997) 324.
[8] J. Kasagi, et al., J. Phys. Soc. Jpn. 73 (2004) 608.
[9] F. Raiola, et al., J. Phys. G 31 (2005) 1141.
[10] J. Cruz, et al., Phys. Lett. B 624 (2005) 181.
[11] T.S. Wang, et al., J. Phys. G, Nucl. Part. Phys. 34 (2007) 2255.
[12] A. Huke, et al., Phys. Rev. C 78 (2008) 015803.
[13] M. Lipoglavšek, et al., Eur. Phys. J. A 44 (2010) 71.
[14] A. Cvetinović, et al., Phys. Rev. C 92 (2015) 065801.
[15] C. Spitaleri, et al., Eur. Phys. J. A 55 (2019) 161.
[16] A. Cvetinovic, et al., Phys. Rev. C 97 (2018) 065801.
[17] K. Czerski, et al., Europhys. Lett. 113 (2016) 22001.
[18] V.M. Bystritsky, et al., Nucl. Phys. A 990 (2019) 29.
[19] V.M. Bystritsky, et al., Eur. Phys. J. A 56 (2020) 60.
[20] S. Ichimaru, H. Kitamura, Phys. Plasmas 6 (1999) 2649.
[21] C. Iliadis, Nuclear Physics of Stars, second, revised and enlarged edition, Wiley-VCH, Weinheim, 2015.
[22] J. Vesić, et al., Eur. Phys. J. A 50 (2014) 153.
[23] M. Lipoglavšek, et al., Phys. Lett. B 773 (2017) 553.
[24] K.U. Kettner, et al., J. Phys. G, Nucl. Part. Phys. 489 (2006) 32.
[25] D.R. Tilley, et al., Nucl. Phys. A 564 (1993) 1.
[26] D.R. Tilley, et al., Nucl. Phys. A 636 (1998) 249.
[27] M. Mayer, SIMNRA User's Guide, Report IPP 9/113, Max-Planck-Institut für Plasmaphysik, Garching, Germany, 1997, https://mam.home.ipp.mpg.de.
[28] J.F. Ziegler, et al., The Stopping and Range of Ions in Matter, Lulu Press Co., Morrisville, NC, 2008, www.srim.org.
[29] G. Alefeld, J. Völkl, Hydrogen in Metals II, Application-Oriented Properties, vol. 29, 1978, p. 81.
[30] C. Rolfs, R.W. Kavanagh, Nucl. Phys. A 455 (1986) 179.
[31] S.C. Snowdon, Phys. Rev. 78 (1950) 299.
[32] K. Spyrou, et al., Eur. Phys. J. A 7 (2000) 79.
[33] S. Engstler, et al., Z. Phys. A, Hadrons Nucl. 342 (1992) 471.
[34] L. Cser, et al., Appl. Phys. Lett. 85 (2004) 1149.
[35] Y. Fukai, The Metal Hydrogen System, Springer, Berlin, 2005 (Chap. 5).
[36] C.P. Slichter, Principles of Magnetic Resonance, Springer, Berlin, Germany, 1990.
[37] L.H. Bennett, et al., J. Res. Natl. Bur. Stand. A, Phys. Chem. 74A (1970) 569.
[38] I. Bakonyi, et al., Phys. Status Solidi B 111 (1982) 59.
[39] K. Tompa, et al., Europhys. Lett. 53 (2001) 79.
[40] M. Deng, et al., Solid State Commun. 150 (2010) 1262.
[41] Ralph H. Petrucci, et al., General Chemistry: Principles and Modern Application, 9th edition, 2007.
[42] B. Hu, Z. Zi, Nucl. Instrum. Methods Phys. Res. B 145 (1998) 288.
[43] C. Tan, et al., Nucl. Instrum. Methods Phys. Res. B 135 (1998) 113.
[44] B. Hu, et al., Nucl. Instrum. Methods Phys. Res. B 160 (2000) 195.
[45] B. Hu, et al., Nucl. Instrum. Methods Phys. Res. B 149 (1999) 395.